Chessboard Focal Plane Array for a CMOS-Integrated Terahertz Camera

Hoogelander, Martijn; Berkel, Sven van; Malotaux, Eduard Satoshi; Alonso-delPino, Maria; Cavallo, Daniele; Spirito, Marco; Llombart, Nuria

DOI
10.1109/TTHZ.2023.3297072

Publication date
2023

Document Version
Final published version

Published in
IEEE Transactions on Terahertz Science and Technology

Chessboard Focal Plane Array for a CMOS-Integrated Terahertz Camera

Martijn Hoogelander, *Student Member, IEEE*, Sven van Berkel, *Member, IEEE*, Eduard Satoshi Malotaux, *Member, IEEE*, Maria Alonso-delPino, *Senior Member, IEEE*, Daniele Cavallo, *Senior Member, IEEE*, Marco Spirito, *Member, IEEE*, and Nuria Llombart, *Fellow, IEEE*

***Abstract*—This article presents the development of a focal plane array (FPA) for terahertz imaging applications with a near diffraction-limited resolution achieved through a very tight sampling of the focal plane. The antenna array is integrated with direct detectors in a 22-nm CMOS technology and operates from 200 to 600 GHz. The tight sampling of the focal plane is realized by using a combination of leaky-wave radiation and a dual-polarized connected array configuration that closely resembles a chessboard. By utilizing both the polarizations in the chessboard design, the number of array elements per unit area is effectively doubled. The geometry of the chessboard array was co-optimized together with that of a silicon elliptical lens to achieve both high aperture efficiency and beam overlap. Measurements in the WR2.2 band of a fabricated demonstrator showed that an aperture efficiency of −4.1 dB was realized at 400 GHz. The average gain roll-off between two diagonally adjacent array elements was measured to be −1.5 dB at 400 GHz. Compared to the reference configuration of an idealized, equivalently sampled hexagonal FPA, the improvement in gain at the edge of coverage yields 1.2 dB, which includes 1.9 dB of ohmic losses in the chessboard array. The agreement between measurements and simulations proved to be within 1 dB from 325 to 475 GHz.**

***Index Terms*—CMOS antenna array, direct detector, focal plane array (FPA), high-resolution imaging, leaky-wave antennas, lens antenna array, passive imaging, terahertz (THz), ultrawideband.**

I. Introduction

THE terahertz (THz) regime offers interesting opportunities to complement or even replace millimeter-wave imagers in commercial applications, such as security screening [1], [2], [3] or automotive imaging [3], [4]. Decreasing the wavelengths by an order of magnitude automatically improves the theoretically achievable resolution by the same factor. Moreover, the higher availability of thermal radiation at smaller wavelengths makes the work toward a fully passive THz imaging system a realistic endeavor, especially when capturing power over a large bandwidth. Thanks to the absence of active components in the front end [3], [5], a passive direct-detection system is more compact and has a substantially lower power consumption compared with an active heterodyne imaging system. A high detector density can likewise be integrated in a single chip at a relatively low cost when fabricated in a commercial silicon technology. To fully exploit the imaging potential at submillimeter wavelengths, there is a need for dense, large-scale focal plane arrays (FPAs) with high aperture efficiencies. Simultaneously, the noise-equivalent power (NEP) of the direct detector needs to be sufficiently low to distinguish the thermal radiation emitted by the subject from the noise injected by the camera itself at room temperatures.

Over the past decade, substantial progress has been made in the scaling of THz FPAs [6] and in minimizing the NEP of antenna-coupled detectors, which now gradually approaches unity pW/$\sqrt{\text{Hz}}$ [7], [8], [9], [10]. It remains difficult, however, to realize FPAs with the element density required to achieve (near) diffraction-limited resolution. Until now, demonstrated THz cameras either have a large element separation [6], [11], leading to blind spots in the field of view (FoV), or suffer from a reduced aperture efficiency [12], [13], [14]. In some works, the penalty in resolution is compensated by employing mechanical scanning mechanisms [15], [16]. A low aperture efficiency, on the other hand, puts more stringent constraints on the detector's performance. This could be tackled by cryogenic cooling of the system [14] or increasing the integration time, at the cost of high system complexity or a low refresh rate, respectively.

In this article, we present the design, implementation, and characterization of an FPA that, thanks to the chessboard architecture, achieves a near diffraction-limited angular resolution and has an aperture efficiency that is comparable to more sparsely sampled FPAs [6] or single-pixel designs [17], [18]. The chessboard array concept, depicted in Fig. 1, was first introduced in [19] and combines multiple concepts from past works on connected arrays [20], [21] and leaky-wave lens antennas [22]. The proposed FPA operates over an ultrawide bandwidth (200–600 GHz) and has two (interleaved) sets of array elements with opposite polarization because of its self-complementary structure.

Manuscript received 26 April 2023; revised 21 June 2023; accepted 6 July 2023. Date of publication 20 July 2023; date of current version 3 November 2023. *(Corresponding author: Martijn Hoogelander.)*

Martijn Hoogelander, Maria Alonso-delPino, Daniele Cavallo, and Nuria Llombart are with the Terahertz Sensing Group, Delft University of Technology, 2628 CD Delft, The Netherlands (e-mail: m.hoogelander@tudelft.nl; m.alonsodelpino@tudelft.nl; D.Cavallo@tudelft.nl; n.llombartjuan@tudelft.nl).

Sven van Berkel was with the Terahertz Sensing Group, Delft University of Technology, 2628 CD Delft, The Netherlands. He is now with the Jet Propulsion Laboratory, California Institute of Technology, Pasadena, CA 91109 USA (e-mail: sven.l.van.berkel@jpl.nasa.gov).

Eduard Satoshi Malotaux was with the Electronic Circuits and Architectures Group, Delft University of Technology, 2628 CD Delft, The Netherlands. He is now with Tusk IC, 2018 Antwerp, Belgium (e-mail: satoshi@malotaux.eu).

Marco Spirito is with the Electronic Circuits and Architectures Group, Delft University of Technology, 2628 CD Delft, The Netherlands (e-mail: M.Spirito@tudelft.nl).

Color versions of one or more figures in this article are available at https://doi.org/10.1109/TTHZ.2023.3297072.

Digital Object Identifier 10.1109/TTHZ.2023.3297072

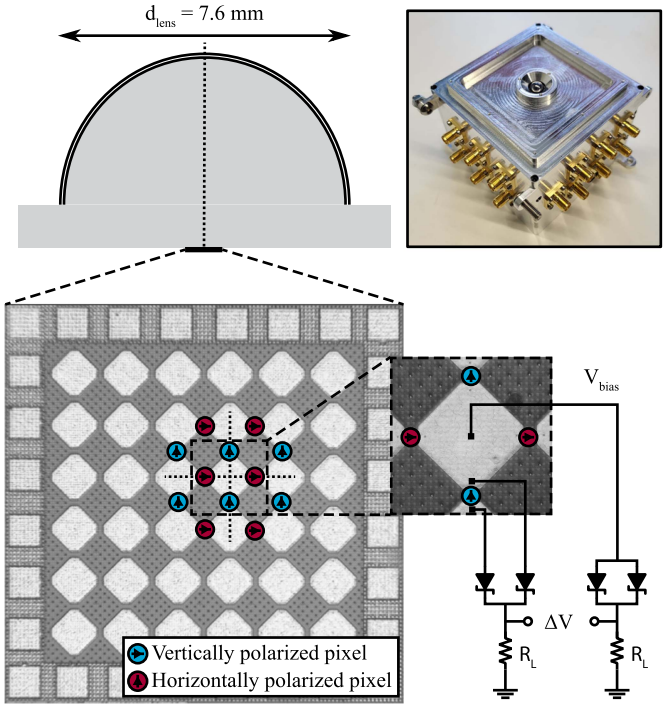

Fig. 1. Overview of the 12-pixel THz camera consisting of an elliptical silicon lens and the CMOS-integrated chessboard FPA. The center of the focal plane is indicated using the dotted axes. The lower inset illustrates the circuitry of the direct detectors, and the upper inset shows the fabricated demonstrator.

The array is designed and implemented in a 22-nm fully depleted silicon-on-insulator (FD-SOI) CMOS technology [23] provided by Global Foundries in the University Partnership Program. The CMOS stratification was exploited to enable the propagation of a wideband, nonresonant leaky-wave mode to illuminate the lens more efficiently [24]. The combination of leaky-wave radiation and polarization reusage results in an FPA of which the individual beams are both highly directive and tightly spaced.

All the elements in the FPA are connected to direct detectors with a topology similar to those in [18]. Although these detectors do not reach state-of-the-art NEP, they are used in this work to enable readout of the antennas and to demonstrate the antenna performance in the framework of a fully integrated THz camera. The excellent capabilities of CMOS for the integration of digital building blocks make it attractive for future system-on-chip solutions. Besides, the use of a deeply scaled FD-SOI CMOS node for this work allows us to address the challenges arising from the strict metal density rules, hereby demonstrating the flexibility of the proposed design.

The rest of this article is organized as follows. In Section II, the challenges of designing tightly sampled FPAs using a conventional but idealized array configuration are investigated. The chessboard array configuration is introduced and studied in Section III to derive the optimum geometry in terms of edge-of-coverage gain. The implementation of the CMOS-integrated demonstrator is discussed in Section IV, after which Section V presents the measurement results. Finally, Section VI concludes this article.

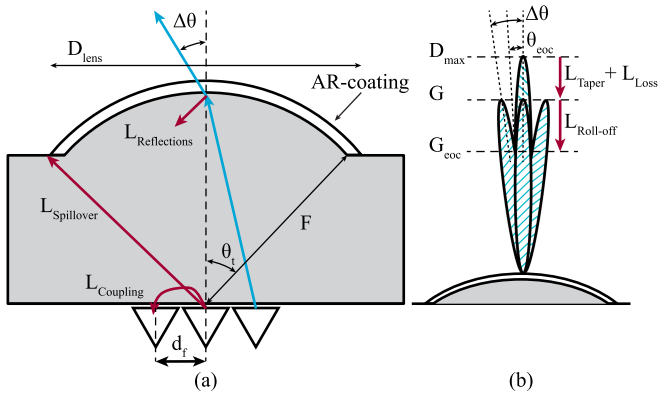

Fig. 2. (a) Generic quasi-optical system where an FPA with sampling periodicity d_f is placed in the focal plane of a dielectric lens with diameter D_{lens} and focal distance F. The beams of adjacent feeds are separated by $\Delta\theta$. (b) Relation between the gain at the edge of coverage G_{eoc} and the directivity of an ideal aperture with the same diameter as the dielectric lens, $D_{\max} = (\pi D_{\text{lens}}/\lambda)^2$.

II. Antenna Parameters and Problem Statement

The simplest solution to realize a multibeam imaging system is the use of a single quasi-optical focusing element (e.g., lens and reflector) combined with a single-beam-per-feed FPA. In Fig. 2, the configuration with a dielectric lens is illustrated. The lens is characterized by its diameter D_{lens} and focal length F, and the FPA is characterized by the sampling periodicity d_{f}. Together, the sampling periodicity and the F-number of the lens ($F_{\#} = F/D_{\text{lens}}$) determine the angular separation of adjacent beams and, equivalently, the angular resolution $\Delta\theta$. The general relationship between the sampling periodicity in the focal plane and the angular resolution can be approximated by [12]

$$d_{\text{f}} = N \cdot 0.5 F_{\#} \lambda_{\text{d}} \leftrightarrow \Delta\theta = N \Delta\theta^{\text{lim}}, \tag{1}$$

where $\lambda_{\text{d}} = \lambda_0/\sqrt{\varepsilon_{\text{r}}}$ is the wavelength in the dielectric lens with relative permittivity ε_{r}, and N is the undersampling factor. For $N = 1$, the focal plane is fully sampled and has a diffraction-limited resolution in an incoherent imaging scenario, i.e., $\Delta\theta^{\text{lim}} = \lambda_0/(2D_{\text{lens}})$ [25]. Unfortunately, a fully sampled FPA yields a low aperture efficiency; thus, the gain and sensitivity of the camera are compromised, as discussed in [12]. For an imaging system to be sensitive over its entire FoV, the gain at the least covered spots, i.e., the edge-of-coverage gain (G_{eoc}), needs to be maximized. This requires a high aperture efficiency, but also a high density of beams such that the roll-off loss is small. To better understand and quantify this design challenge, this section explores the performance metrics used to compare different FPA designs in terms of sampling periodicity and aperture efficiency.

Let us study the losses and beam spacing of an idealized FPA of circular, electrically large feeds with a uniform current distribution, arranged in a hexagonal grid with sampling configurations $N = 1, 2, 4$. At this stage, any losses associated with reflections and mutual coupling between the feed elements are not considered. Table I summarizes the angular resolution beam roll-off at $\theta_{\text{eoc}} = \Delta\theta/\sqrt{3}$ (i.e., the least covered point in a hexagonal grid) and losses due to spillover and aperture field tapering of this geometry. The tradeoff between resolution and

TABLE I
FEED SAMPLING TRADEOFF BETWEEN RESOLUTION AND EFFICIENCY FOR UNIFORM APERTURE FEEDS

Sampling	Resolution $\Delta\theta$ [rad]	$L_{\text{roll-off}}$ [dB]	$L_{\text{Spillover}}$ [dB]	L_{Taper} [dB]	ΔG_{eoc} [dB]
$0.5F_{\#}\lambda_d$	$\lambda_0/(2D)$	0.91	8.16	0.00	9.1
$1F_{\#}\lambda_d$	λ_0/D	3.65	3.27	0.04	7.0
$2F_{\#}\lambda_d$	$2\lambda_0/D$	13.18	0.81	0.80	14.8

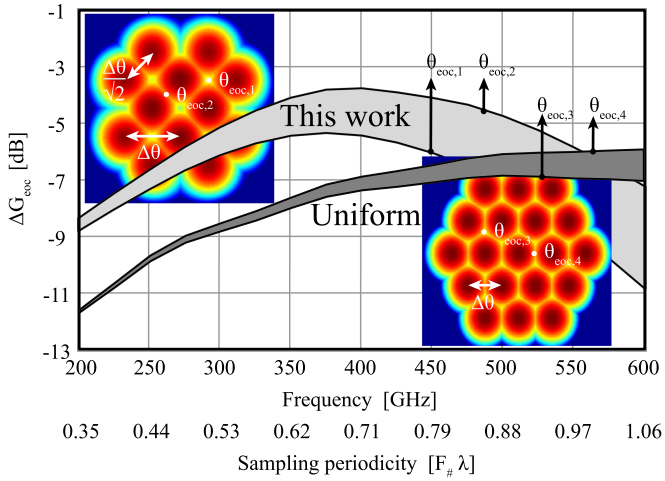

Fig. 3. ΔG_{eoc} versus frequency and sampling periodicity of an ideal hexagonal grid of uniform circular feeds illuminating a reflector system (dark gray area) and of a chessboard connected array illuminating a silicon lens (light gray area). The lower bounds represent the least covered spots in the grids (e.g., the E-plane for the chessboard array), whereas the upper bounds represent the spots between the beams that are closest to each other.

aperture efficiency can be clearly recognized. The sum of the roll-off and other losses is also shown. This metric represents the difference between the ideal gain of the aperture and the gain at the edge of coverage; it is defined as:

$$\Delta G_{\text{eoc}} = L_{\text{Taper}} - L_{\text{Roll-off}} - L_{\text{Loss}}. \tag{2}$$

The individual contributions to ΔG_{eoc} are visualized in Fig. 2. They include the tapering loss $L_{\text{Taper}} = D/D_{\max}$, which relates the directivity D of the lens antenna with that of an ideal aperture ($D_{\max}$), the roll-off between two beams $L_{\text{Roll-off}}$, and the combination of all other losses $L_{\text{Loss}} = G/D$, which relates the antenna gain G to its directivity. In Table I, only the spillover is included in L_{Loss}, but in next sections, other contributions are also included. The metric ΔG_{eoc} provides a fair comparison between different FPA architectures, since both the aperture efficiency and the angular separation of the beams are considered.

From Table I, it can be determined that a hexagonal FPA with a sampling periodicity of $d_{\text{f}} = 1F_{\#}\lambda_{\text{d}}$ yields the optimal ΔG_{eoc} of -7 dB. The ΔG_{eoc} of the ideal hexagonal FPA is shown as a function of sampling periodicity (or, equivalently, frequency) in Fig. 3 using the dark gray area. The following section presents the design and optimization of a chessboard array configuration, of which ΔG_{eoc} (not considering ohmic losses) is shown in Fig. 3 using the light gray area.

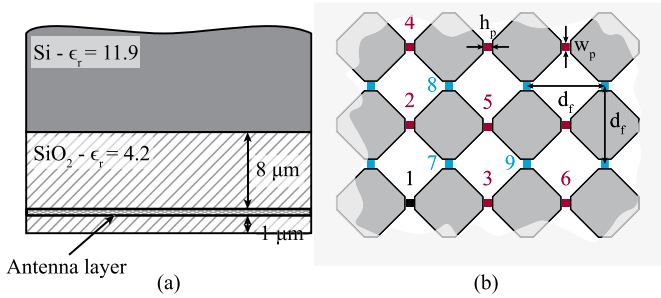

Fig. 4. Configuration of the considered chessboard array. (a) Antenna stratification, (b) Connected array of tapered dipoles. The sampling periodicity in the horizontal and vertical dimensions is $d_{\text{f}} = 1 \cdot F_{\#}\lambda_{\text{d}}$ at 400 GHz, and the port dimensions are fixed to $w_{\text{p}} = 20\ \mu$m and $h_{\text{p}} = 15\ \mu$m for both the polarizations.

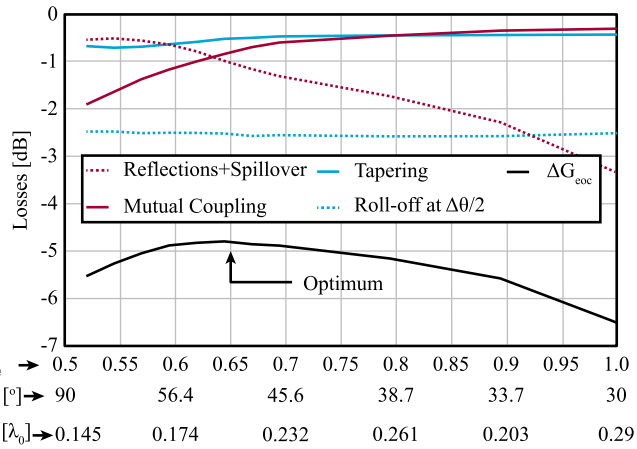

Fig. 5. Difference in the gain of an ideal aperture and the gain at the edge of coverage, ΔG_{eoc}, in the H-plane of the chessboard FPA feeding an elliptical silicon lens. The sampling condition was set to $d_{\text{f}} = 1 \cdot F_{\#}\lambda_{\text{d}}$ in the vertical and horizontal dimensions. The results are plotted as a function of $F_{\#}$ and include the different loss contributions. Optimal ΔG_{eoc} is obtained for $F_{\#} = 0.65$.

III. DESIGN OF THE CHESSBOARD FPA

In this section, we describe the design of a chessboard FPA operating between 200 and 600 GHz and implemented in a 22-nm FD-SOI CMOS process. From the perspective of passive imaging at submillimeter wavelengths, this frequency range allows for operation over a few hundred gigahertz of bandwidth but avoids the large atmospheric attenuation that is present beyond 1 THz [2]. Connected arrays feeding dense dielectric lenses can achieve ultrawideband operation while realizing an efficient illumination of the lens [20], [21]. However, when the feeds are small in terms of the wavelength, they also introduce a significant mutual coupling. In [20], the mutual coupling is analyzed as a function of the wavelength, but the tradeoff in terms of ΔG_{eoc} was not discussed explicitly. Here, we extend these initial studies to a chessboard connected array configuration in order to maximize ΔG_{eoc} at the central frequency.

The chessboard array under consideration is shown in Fig. 4. The illustrated stratification approximates the 22-nm FD-SOI CMOS process and consists of a simplified silicon dioxide (SiO_2) layer with an average relative permittivity $\varepsilon_{\text{r}} = 4.2$ and the bulk silicon. The antenna layer is embedded in the SiO_2 and

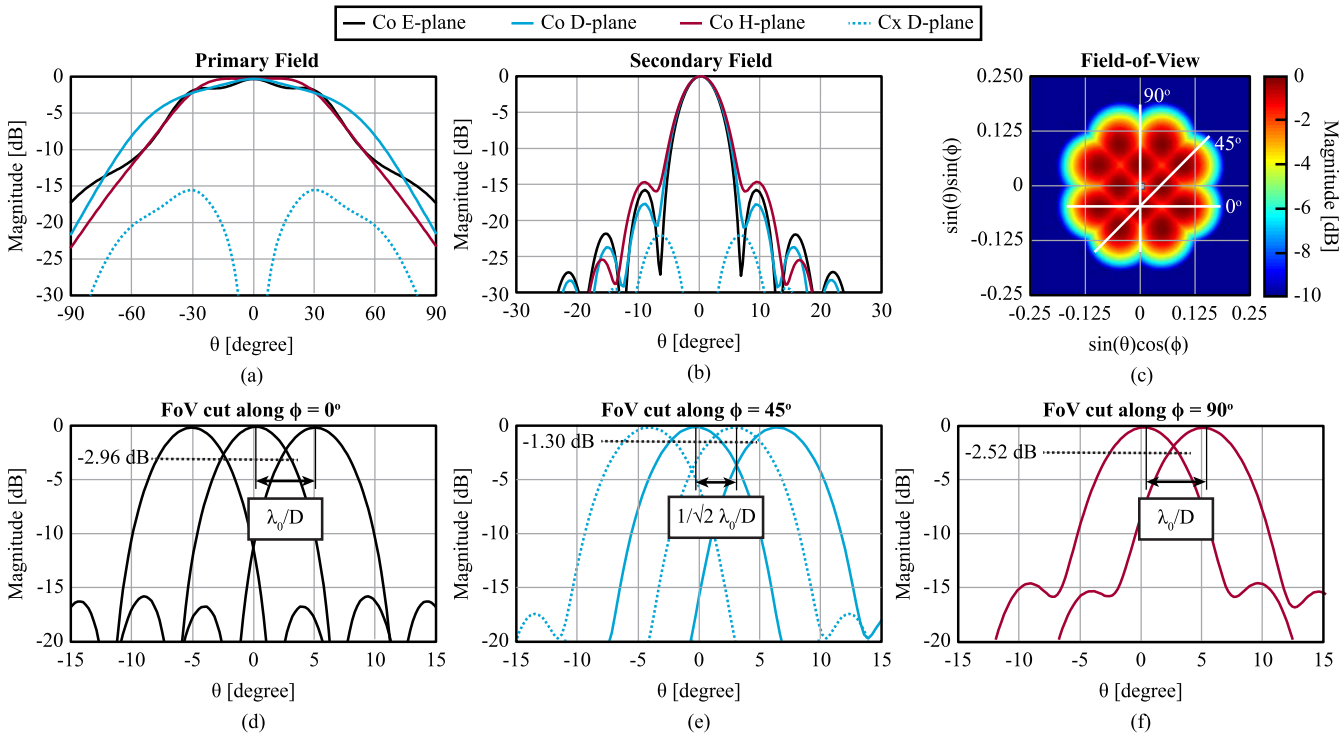

Fig. 6. Simulated radiation patterns at 400 GHz of a chessboard FPA configuration with $F_{\#} = 0.65$ and $d_f = 1 \cdot F_{\#}\lambda_d$. (a) Primary radiation pattern. (b) Secondary radiation pattern. (c) 2-D plot of the array FoV. (d) E-plane pattern along $\phi = 0^\circ$. (e) D-plane pattern along $\phi = 45^\circ$ (D-plane). (f) H-plane pattern along $\phi = 90^\circ$.

separated from the semi-infinite silicon half-space (i.e., the bulk silicon and the lens) by approximately 8 μm. For simplification, the thin oxide box of the FD-SOI process is omitted. In [24], it is shown that a slightly enhanced leaky-wave radiation can be achieved in this stratification. The same technique is also used in this work to realize a higher gain of the feed elements and, consequently, higher ΔG_{eoc}. The array elements consist of dipoles that are tapered with an angle of 45° to realize a self-complementary geometry that resembles a chessboard, as can be recognized in Fig. 4(b). As such, two polarizations can be utilized equivalently, and the effective sampling periodicity is reduced by a factor of $\sqrt{2}$ along the diagonal.

To obtain the optimum geometry of the lens and FPA for maximum ΔG_{eoc}, $F_{\#}$ of the lens is changed while keeping the focal plane sampling periodicity constant in terms of $F_{\#}\lambda_d$. The simulated array consists of $N_{\text{ports,H}} = 5 \times 5$ horizontally polarized ports [red in Fig. 4(b)] and $N_{\text{ports,V}} = 4 \times 6$ vertically polarized ports [blue in Fig. 4(b)], yielding a total of 49 ports. The embedded primary radiation patterns inside the silicon lens were obtained from full-wave simulations in CST Studio Suite and imported into an in-house physical optics tool [26] to compute the patterns radiated from the lens. In Fig. 5, the different loss contributions are shown as a function of $F_{\#}$, the truncation angle of the primary fields $\theta_t \approx \arcsin(1/(2F_{\#}))$ [see Fig. 2(a)], and feed separation d_f. As can be seen, a larger $F_{\#}$ decreases the truncation angle of the lens and increases the spacing of the elements. Although the latter results in lower mutual coupling losses, the smaller truncation angle θ_t leads to increased spillover losses. The tapering loses are only slightly better for a larger $F_{\#}$. The roll-off loss, here shown for the H-plane, remains practically constant as function of $F_{\#}$ as would be expected. The small changes that can be observed are due to the variation in tapering efficiency. It can be observed that optimum ΔG_{eoc} is obtained approximately at the point where the mutual coupling losses are equal to the spillover losses, at $F_{\#} = 0.65$.

The primary radiation pattern of a single element in the optimized chessboard FPA is shown in Fig. 6(a). Despite the array having a self-complementary layout, the radiation patterns are asymmetric in different planes because the FPA is placed between a dielectric and air [27]. The corresponding secondary radiation pattern outside the elliptical lens is shown in Fig. 6(b). In order to evaluate the beam spacing in different planes, the multibeam radiation patterns were evaluated in a part of the array consisting of 2×3 horizontally and 3×2 vertically polarized elements. Fig. 6(c) shows the normalized beams of these elements in a 2-D surface plot. In this figure, azimuthal cuts are defined for the main and diagonal planes, along which the radiation patterns are given in Fig. 6(d)–(f). The main planes yield the least covered spots in the rectangular grid. In these planes, the edge of coverage is located at $\theta_{\text{eoc}} = \Delta\theta/2 = 2.84^\circ$, and the roll-off loss is between −2.5 and −3 dB. Along the diagonals, an enormous improvement in roll-off loss can be observed, which is only −1.3 dB and located at $\theta_{\text{eoc}} = \Delta\theta/\sqrt{2} = 2.01^\circ$.

The light gray area in Fig. 3 shows ΔG_{eoc} as a function of the frequency for the optimized geometry. Note that the sampling periodicity on the secondary x-axis is given with respect to the diagonal planes for the chessboard array. When designing for the

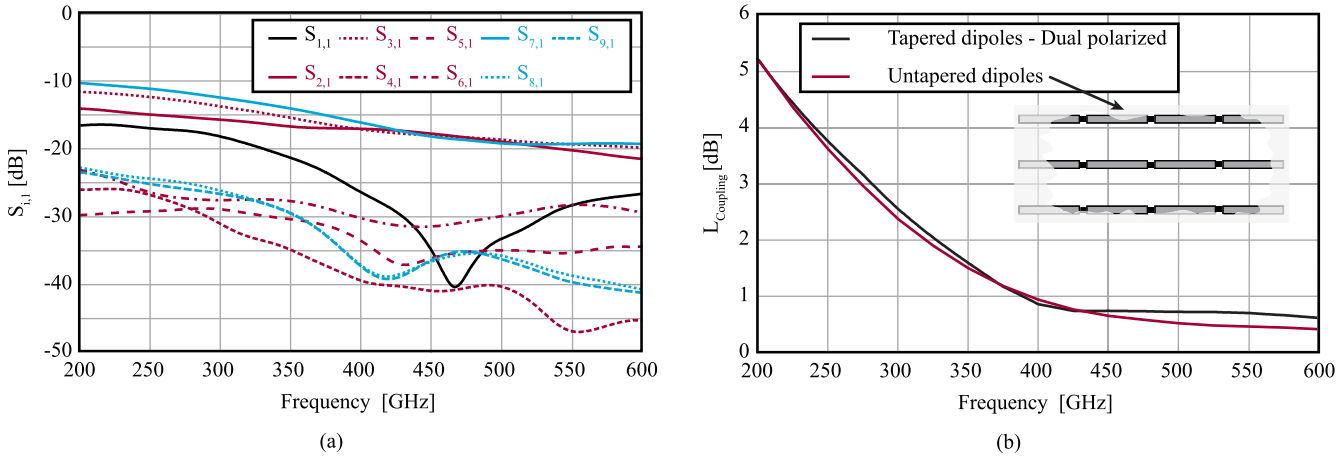

Fig. 7. (a) Simulated mutual coupling between the chessboard FPA ports from Fig. 4. (b) Total coupling losses of the chessboard array as calculated using (3). The reference case of a connected array of untapered dipoles is also shown. Both the arrays are sampled with $d_f = 1 \cdot F_{\#}\lambda_d$ along the horizontal and vertical dimensions at 400 GHz, with $F_{\#} = 0.65$. The feeds are terminated with Z_{port} =100 Ω.

same resolution at a sampling periodicity of $d_f = 1/\sqrt{2} \cdot F_{\#}\lambda_d$, an improvement of 3.5 dB is achieved with respect to the ideal hexagonal FPA. Although the array is not optimized for diffraction limited resolution (i.e., $d_f = 0.5 \cdot F_{\#}\lambda_d$), the chessboard configuration also features a 3.7-dB improvement in ΔG_{eoc} in this scenario.

Finally, we take a closer look at the mutual coupling. Fig. 7(a) shows the S-parameters versus frequency for the optimal FPA geometry, when the central element is excited. This central element corresponds to port 1 in Fig. 4(b). Note that only the top right quadrant of the simulated array is depicted in this figure. The red curves represent the antenna feeds with the same (horizontal) polarization, whereas the blue curves represent the vertically polarized feeds. The S-parameters are normalized to a port impedance of $Z_{\text{port}} = 100\ \Omega$. It can be observed that the dominant contributors are $S_{2,1}$, $S_{3,1}$, and $S_{7,1}$, which correspond to all the directly neighboring ports (irrespective of their polarization). The coupling to the remaining ports is lower than −22 dB over the full frequency range. The small differences between equally polarized array elements placed at radially symmetric positions can be explained by the nonsymmetric radiation pattern of the array elements [see Fig. 6(a)].

The total mutual coupling losses, L_{Coupling}, are calculated from the reference point of the central element by using

$$L_{\text{Coupling}} = 1 - \sum_{i=2}^{N_{\text{ports}}=49} |S_{i,1}|^2, \tag{3}$$

in which $S_{i,1}$ are the S-parameters related to the central element. Evaluating (3) as a function of frequency leads to the result shown in Fig. 7(b), which shows that a sampling periodicity of $d_{\text{f}} < \lambda_0/5$ results in high mutual coupling losses. These losses are, however, still significantly lower than the spillover losses when using nonoverlapping uniform feeds in a hexagonal grid as evident from inspecting Table I. As a reference, Fig. 7(b) also provides the case of a connected array of untapered dipoles with the same sampling periodicity operating in only a single polarization. One might expect higher mutual coupling losses for the dual-polarized array, since Fig. 7(a) showed that $S_{7,1} \approx S_{3,1}$. However, the mutual coupling with the neighboring element along the direction of the dipole in the untapered array would have been approximately twice as high, resulting in almost identical total mutual coupling losses. Moreover, when utilizing both the polarizations in the chessboard array, the sampling periodicity is reduced by a factor of $\sqrt{2}$ with respect to the (single-polarized) array of untapered dipoles.

IV. Chessboard FPA Demonstrator

A demonstrator of the chessboard FPA with integrated direct detectors was developed in a commercial 22-nm FD-SOI CMOS process from Global Foundries, which contains ten copper layers with one ultrathick layer. An image of the chip is included in Fig. 1. The silicon lens available for the demonstrator is repurposed from a previous project and has a focal number slightly below the optimum value ($F_{\#} = 0.56$). The lens has a diameter of 7.56 mm ($10\lambda_0$ at 400 GHz) and is coated with a layer of parylene-C to minimize reflection losses. The focal plane in the prototype is sampled with $d_{\text{f}} = 1 \cdot F_{\#}\lambda_d = 130$ µm at 363 GHz in the main planes. When considering both the polarizations, this corresponds to an effective sampling of $d_{\text{f}}^{\text{eff}} = 1/\sqrt{2} \cdot F_{\#}\lambda_{\text{d}} = 92$ µm along the diagonal. The gap dimensions of the dipoles are the same as in Fig. 4, with $w_{\text{p}} = 20$ µm and $h_{\text{p}} = 15$ µm.

Each of the 60 feeding points in the chessboard array is connected to a differential pair of Schottky barrier diodes (SBDs) biased in the square-law region to realize the power detection. The current response from the diodes is converted to a voltage using a 4-kΩ resistor located at the common node, as shown in Fig. 8(a). A reference branch, not connected to the antenna, is also integrated to realize a pseudodifferential readout. Biasing of the devices is done via connections placed at the center of the chessboard antennas. The complete detector circuit can be recognized in Fig. 8(a), but a simplified illustration is also given in Fig. 1. The operational principle and performance of highly similar direct detectors (with identical SBDs) were fully

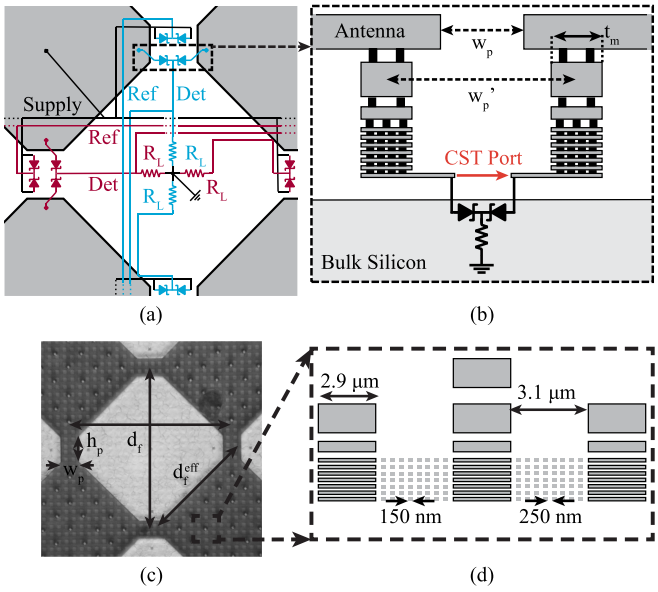

Fig. 8. (a) Architecture and routing of the direct detectors per array unit cell. (b) Vertical transition from the antenna to the detector. (c) Geometry and spacing of single metal antenna patch. (d) Close-up of the metal tiling in layers M1–M7 and the three top layers to fulfill the metal density rules. Note that neither (b) nor (d) is to scale, especially in the vertical dimension.

evaluated in [18] in terms of responsivity, noise, and NEP. The results from this previous work will be used in Section V to extract the antenna efficiency of the chessboard FPA from the system-level response.

Of all the 60 feed gaps, only 12 (six per polarization) can be readout via individual lines to the bonding pads. This implementation was chosen to minimize additional circuitry on the chip (e.g., for multiplexing), and therefore, we were limited by the area available for bond pads around the array perimeter. The connected 12 array elements are highlighted in Fig. 1. Although the other elements cannot be accessed, they are also biased to maintain uniform matching conditions within the array. In Fig. 8(a), it is shown how the diode pairs and resistors are distributed within each array unit cell and how their interconnections are (locally) routed. The placement of these lines underneath the metal antenna pads is optimized via electromagnetic simulations to minimally interfere with the radiation patterns of the antenna elements. Although not depicted as such in the schematic, lines corresponding to the supplies and readout run mostly on the top of each other in different layers of the metal stack rather than next to each other, such that their total cross section to the radiated fields is minimal.

A major design challenge when designing integrated systems in ultrascaled CMOS technologies is to comply with the strict design rule check (DRC) for metal densities. Usually, minimum sized metal tiles are distributed over the layout as a final step before fabrication to make it comply with the density rules. Fully incorporating this rule into the design process, by making parameterized scripted unit cells completely DRC-clean, ensures that the electromagnetic effects of the metal tiling can be accounted for and optimized during the design phase of the component. The metal tiling was designed in all ten metal layers for a minimal change in effective permittivity and low losses using the methods presented in [24]. A simplified depiction of the metal tiles is illustrated in Fig. 8(c) and (d). In the ultrathick top layer (i.e., antenna layer), they are of size 1.4 µm with a spacing of 14.4 µm, whereas all other metal layers contain 2.9 µm tiles spaced 3.1 µm apart. The lower layers (M1–M7) also have a smaller tiling of 150 nm with 250-nm spacing. In order to efficiently simulate the effects of this complex stratification in CST, the layers that include the DRC tiling were replaced by equivalent anisotropic layers, of which the relative permittivity and tangent delta tensors were determined using the in-house tool [28] based on the theory in [29]. As shown in [24], the ohmic losses in these layers are only 0.2 dB over the entire frequency band. The increase of the (effective) relative permittivity of the medium does result in a slightly lower directivity of the antenna elements with respect to the ideal case (i.e., without tiling). The (ohmic) losses in the array implementation are plotted in Fig. 9(a). Besides the aforementioned contribution, they also include the front-to-back ratio, conductor losses, and the losses in the low resistivity silicon (the CMOS chip has a thickness of 255 µm).

The input reactance to the diode pair is capacitive of nature [18]. To improve the impedance matching with the antenna, the inductive behavior of the vertical transition needs to be carefully optimized. These vertical transitions were included in the CST model of the array by placing the port in between the connections to the diodes [see Fig. 8(b)]. By combining the resulting antenna input impedance with the impedance characteristics of the SBDs obtained from simulations using the process design kit (PDK), the positions of the transitions were tuned for a broadband impedance match. The effect of the optimized vertical transitions on the antenna impedance is shown in Fig. 9(b). Unfortunately, since the SBDs are identical to those used in [18] and the array was fabricated in the same run, the devices suffer from the same increased series resistance (135 Ω instead of 10 Ω) and junction capacitance (20 fF instead of 8 fF) with respect to the PDK values. As such, they will suffer from a significantly lower responsivity and higher NEP than one would expect from a typical SBD detector [10]. In addition, the conjugate matching condition anticipated from simulations was not fully achieved. The input impedance of the SBD pair shown in Fig. 9(b) is corrected for this mismatch between physical devices and the PDK using empirical data. The impedance matching efficiency is shown in Fig. 9(a).

With all loss contributions introduced, we can define a more rigorous expression for the aperture efficiency of the antenna. It comprises all the aforementioned loss mechanisms (with the exception of the impedance matching) and is given by

$$\eta_{\mathrm{ap}} = \eta_{\mathrm{Feed}}\eta_{\mathrm{SO}}\eta_{\mathrm{Ref}}\eta_{\mathrm{Taper}}\eta_{\mathrm{MC}}, \tag{4}$$

where η_{Feed} represents the efficiency of the feed elements [see Fig. 9(a)], η_{SO} is the spillover efficiency, η_{Ref} is reflections at the lens–air interface, η_{Taper} is the tapering efficiency, and η_{MC} is the losses due to mutual coupling between the elements. The aperture efficiency is shown in Fig. 9(c) as a function of frequency.

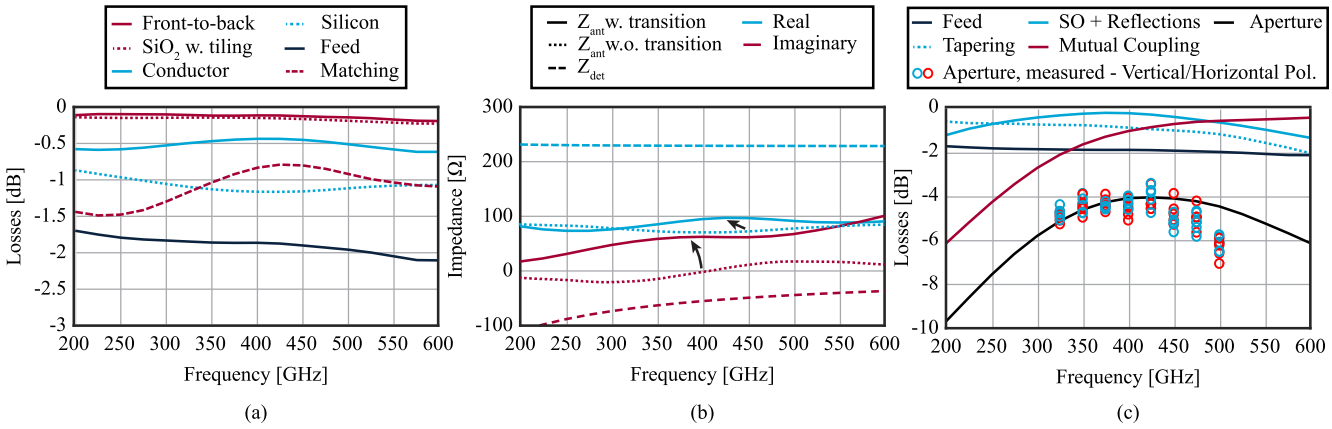

Fig. 9. Simulated performance of the chessboard array prototype as a function of frequency. (a) Losses introduced by the dielectric layers, metals, and front-to-back ratio. In the total losses in the feed, all the terms are included except the impedance matching. (b) Input impedance of the antenna (with and without the vertical transition) and the detector at a bias voltage of 1 V. (c) Aperture efficiency with all its individual contributions. The blue and red circles represent the aperture efficiency extracted from measurements of vertically and horizontally polarized elements, respectively.

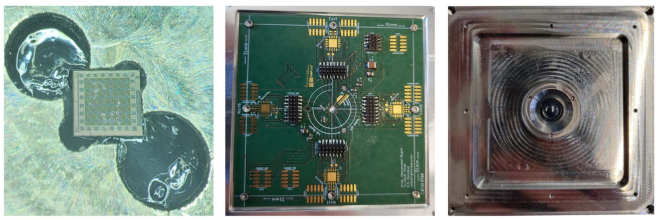

Fig. 10. (a) Photograph of the chessboard FPA chip in the alignment cavity. (b) Readout board. (c) Aluminum holder with the silicon lens.

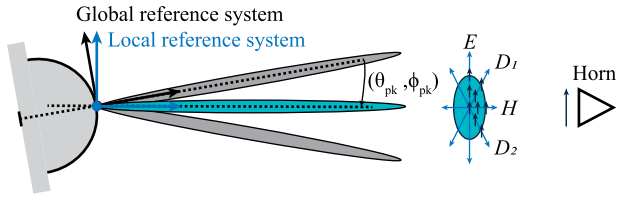

Fig. 12. Used reference systems: the global reference system for alignment to the horn and the local reference system for individual beam pattern measurements. The measured cuts and polarization of the aligned beam (in blue) are highlighted in the frontal view of the beam, shown between the beam and the horn.

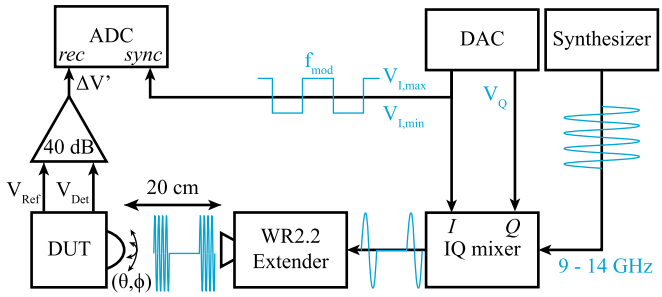

Fig. 11. Simplified schematic of the test bench used to characterize the chessboard array demonstrator.

V. Experimental Validation

For the experimental validation of the chessboard FPA, the fabricated CMOS chip was glued to the backside of the silicon lens and wire bonded to a printed circuit board for biasing and readout. An aluminum holder was fabricated with cavities on either side to contain and align the chip and lens. To make the demonstrator more robust and to shield it from ambient noise, an aluminum casing was designed and manufactured, as shown in Fig. 1. The assembly steps are shown in Fig. 10.

The main performance metrics of interest (i.e., radiation patterns, directivity, aperture efficiency, and beam overlap) of the demonstrator were all extracted from the voltage response of the 12 accessible array elements. The measurements were performed in the WR2.2 band using the setup illustrated in Fig. 11. A more detailed description of this test bench is provided in [30]. The lens was illuminated using a 20-dB standard gain horn antenna excited by a frequency extender module from VDI. The signal for driving the extender module was modulated (i.e., chopped) to achieve a high measurement dynamic range (DR). The modulation shifts the detector response from dc to higher frequencies, hereby minimizing the impact of Flicker noise injected by the embedded devices. In [18], it was estimated that the $1/f$-corner frequency of the direct detectors lies in the low-megahertz range. The chopping operation was implemented using an in-phase–quadrature (IQ) mixer driven by a square wave from an NI 200-MS/s digital-to-analog converter (DAC) card. To acquire the output voltage, a 100-MS/s analog-to-digital converter (ADC) card from NI was used in combination with a 40-dB low-noise instrumentation amplifier (LNIA). The LNIA has a 1.5-nV/$\sqrt{\text{Hz}}$ input-referred noise floor and a half-power bandwidth of 8 MHz. Since the chip does not contain any multiplexing circuitry, the array elements have to be either readout sequentially (possibly with external multiplexing) or in parallel. To keep the measurement setup simple and compact, and/or to prevent additional noise contributions from external multiplexing circuitry, the choice was made to characterize the array elements sequentially.

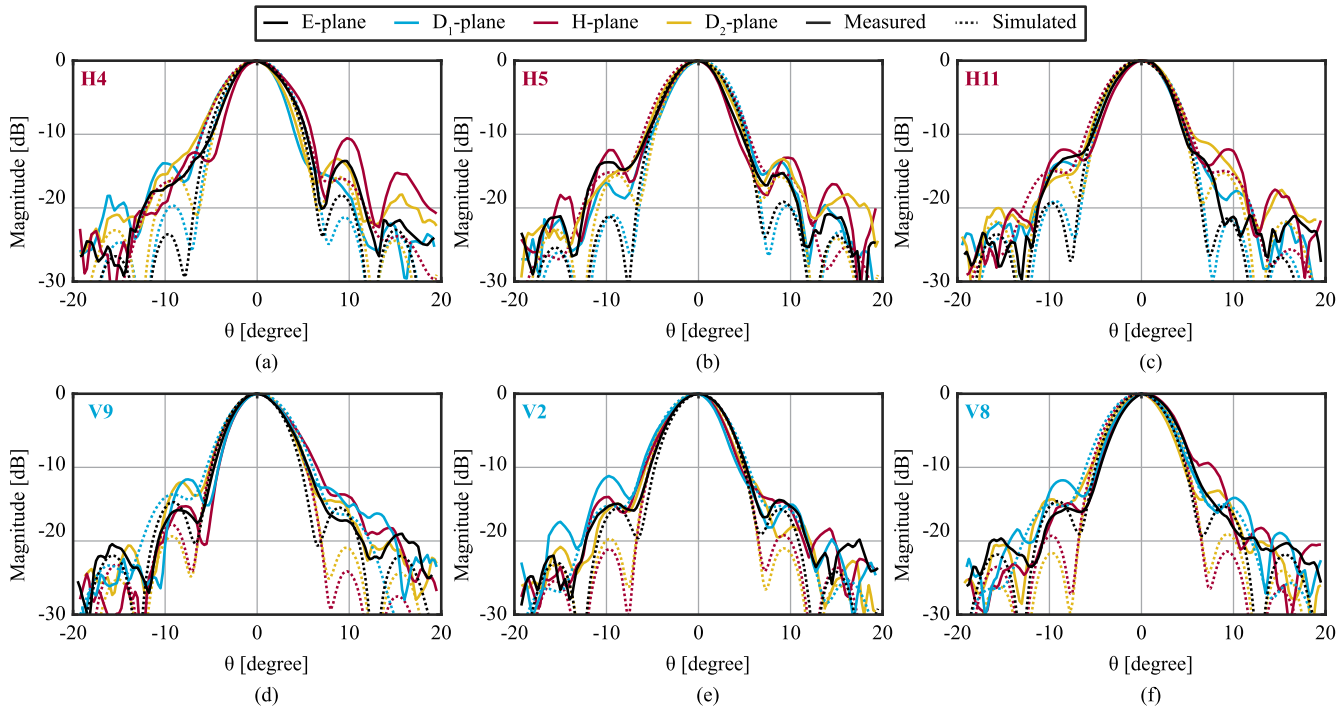

Fig. 13. Measured and simulated patterns of individual elements in their local reference systems at 400 GHz. (a)–(c) Measured radiation patterns of three horizontally polarized elements. (d)–(f) Measured radiation patterns of three vertically polarized elements. Leftmost figures correspond to array elements located near the edges of the 12-pixel subarray.

A. *Individual Beam Patterns and Directivity*

In order to measure the radiation patterns of individual array elements, the prototype was mounted on a gimbal with two rotation axes using a 3-D printed bracket. The use of a gimbal allowed us to directly measure the patterns of different array elements in a (local) spherical coordinate system. The phase center of the lens antenna (i.e., the tip of the lens) was placed at the center of rotation of the gimbal and placed at a distance 20 cm from the horn, which remained in the same position for all the measurements.

The patterns of six active elements in the prototype were measured, three per polarization. For each element, alignment to the horn was performed by searching for the maximum detector response at 400 GHz along the two rotation axes. The angular location corresponding to the beam maximum was saved in a global reference system in UV coordinates (i.e., latitude $U = \sin\theta\cos\phi$, longitude $V = \sin\theta\sin\phi$). The origin of this global reference system corresponds to the broadside direction of the lens antenna. After alignment to an individual array element, a UV reference system local to its beam maximum was constructed to measure the radiation pattern along four azimuthal cuts (E-, H-, and two D-planes) over a range of $\pm 20^\circ$. An illustration of the global and local reference systems and the four considered cuts is shown in Fig. 12.

Because the horn only supports a single polarization and the gimbal just has two rotation axes, the test bench allows us to characterize only the copolarized field component [31] in the four measured planes. Likewise, only half of the array elements (either horizontally or vertically polarized) can be measured at a time. To measure the radiation patterns of the other array elements, another 3-D printed mounting bracket was used to rotate the demonstrator around a third axis within the gimbal.

Following from the study in [30], the modulation frequency was set to 1 MHz for the pattern measurements. This modulation frequency yields maximum measurement DR when biasing the array with a voltage of 1 V. For further enhancement of the DR, the output signal was averaged over a total time of 1 s per frequency and orientation. The DR obtained in this test bench was around 30 dB, which includes the over-the-air spreading losses.

Since the voltage response is a linear function of the received power, the radiation patterns can be reconstructed directly from the voltage response at different gimbal orientations. The measured and simulated radiation patterns along the four considered cuts of all six measured elements within the array are shown in Fig. 13 in their local reference systems at a frequency of 400 GHz. As can be seen, the main lobes of the elements have a good agreement with simulations. The patterns of a central element at different frequencies were shown in [30] and are not reported again in this article.

The directivity of the considered elements was determined as a function of frequency using the patterns along the measured cuts. As explained in [30], the measured radiation patterns at the extremes of the WR2.2 band had to be truncated to $|\theta| \approx 10^\circ$ and $|\theta| \approx 12^\circ$ such that the noise floor is excluded from the directivity computation. The resulting directivity is shown in Fig. 14, where the circles correspond to the directivity of the measured elements. The solid and dotted lines represent, respectively, the simulated directivity when integrating over the complete simulated 2-D pattern and when matching the integration range

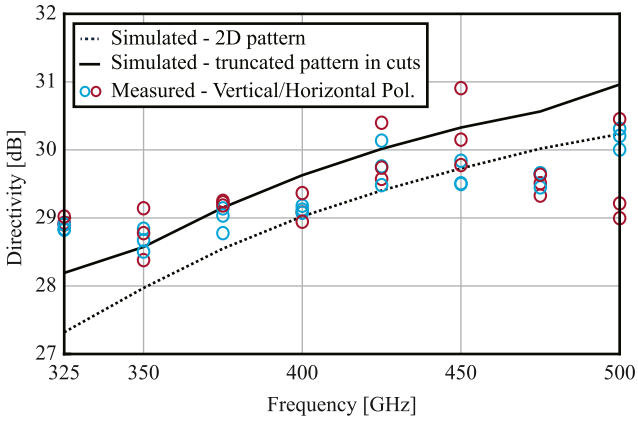

Fig. 14. Measured and simulated directivity of the elements from Fig. 13 as a function of frequency. The blue and red dots correspond to measured vertically and horizontally polarized elements, respectively. To provide a good benchmark to the measurements, the simulated directivity was calculated using the complete 2-D pattern and using the same truncation/cuts as in the measured scenario.

to the cuts and truncation of the measurements, which provides a better benchmark. As can be observed, the match between the simulated and measured directivity of all array elements is within 1 dB up to 450 GHz. The impact of the standing waves in the test bench was evaluated in [30] and gives a directivity variation of around ±0.5 dB. The directivity at the lower end of the WR2.2 band is a bit higher than expected, possibly due to reradiated power that is reflected from the diodes, and/or the higher mutual coupling at these frequencies [21]. Considering the operational frequencies and the tolerances from the lens fabrication (±20 µm), chip-to-lens alignment (± 50 µm laterally and ±40 µm longitudinally), as well as the unavailability of techniques, such as time gating to remove standing wave effects, a good match between simulations and measurements is achieved over the entire WR2.2 band.

B. Aperture Efficiency

As a result of the integration of direct detectors with the antenna array, it is not possible to perform antenna gain measurements directly. Instead, the gain is obtained via the aperture efficiency, which relates the antenna gain to its directivity. The aperture efficiency, in turn, is obtained from the characterization of the system-level responsivity of the array elements. The voltage system responsivity, $\Re_{\mathrm{v,sys}}$, describes the conversion of power incident on the lens aperture to a voltage change at the detector output of a single array element. In this specific setup, it is defined as

$$\Re_{\mathrm{v,sys}} = \frac{\Delta V'}{P_{\mathrm{in}} G_{\mathrm{LNIA}}} = \frac{(4\pi R)^2 \Delta V'}{\lambda_0^2 P_{\mathrm{src}} G_{\mathrm{horn}} D_{\mathrm{max,lens}} G_{\mathrm{LNIA}}}, \quad (5)$$

in which $\Delta V'$ is the voltage swing at the output of the LNIA, arising from the ON–OFF switching of the extender module, P_{in} is the power incident on the lens, and G_{LNIA} is the gain of the LNIA. The incident power can be calculated from the power radiated from the horn antenna during the ON-time of the extender module (P_{src}), the gain of the horn (G_{horn}), the path loss over a distance R between the horn and the lens (i.e., 20 cm), and the maximum

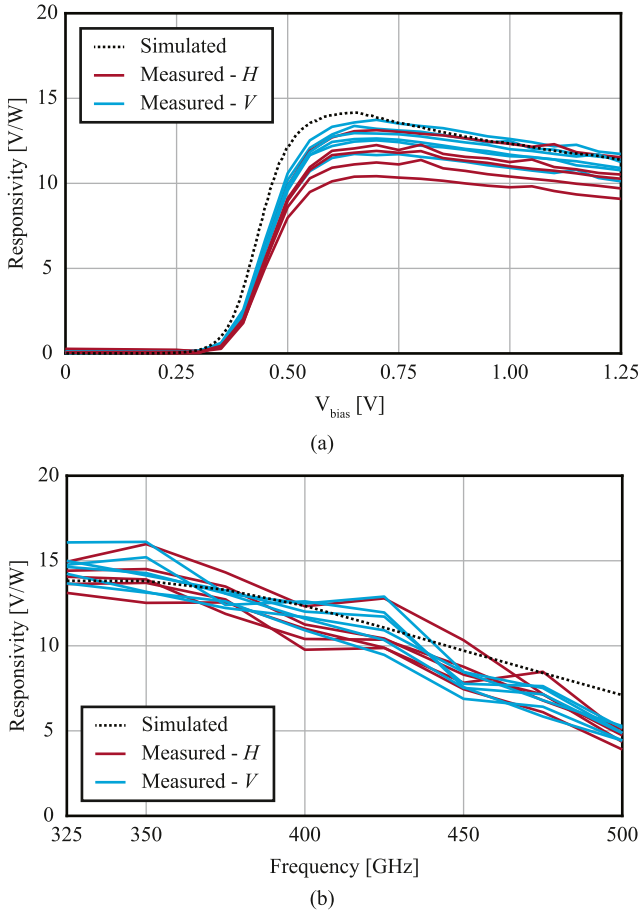

Fig. 15. Measured and simulated system responsivity (a) as a function of bias voltage at 400 GHz and (b) versus frequency at a fixed bias voltage of 1 V.

theoretical directivity of the aperture of the lens ($D_{\mathrm{max,lens}}$). The voltage swing can be calculated from the fundamental tone in the double-sided frequency spectrum of the output voltage using the relation $\Delta V' = \pi V_{\mathrm{out,LNIA}}(f_{\mathrm{mod}})$. The system responsivity includes all the losses from the lens aperture to the output, as well as the rectifying action of the SBDs. Therefore, it can also be calculated with simulated performance metrics using

$$\Re_{\mathrm{v,sys,sim}} = \eta_{\mathrm{ap}} \eta_{\Omega} \Re_{\mathrm{v,det,sim}} \quad (6)$$

where η_{ap} is the aperture efficiency as defined in (4), η_{Ω} is the impedance matching efficiency between the antenna and SBD pair, and $\Re_{\mathrm{v,det,sim}}$ is the (simulated) voltage responsivity of the detector. This responsivity was thoroughly characterized in [18] of similar detectors that were fabricated on the same silicon die as the array and contain identical SBDs. Therefore, we can equate (5) and (6) and use the results from [18] to extract the aperture efficiency from the system responsivity per array element.

While measuring $\Re_{\mathrm{v,sys}}$, the orientation of the gimbal was fixed to the angular locations corresponding to the individual beam maxima. In addition, the modulation frequency was decreased to 55 kHz to ensure that the system response at low bias voltages was not affected by the modulation, and thus the measurement precision is maintained [30]. The measured and simulated system responsivity of the active elements is shown

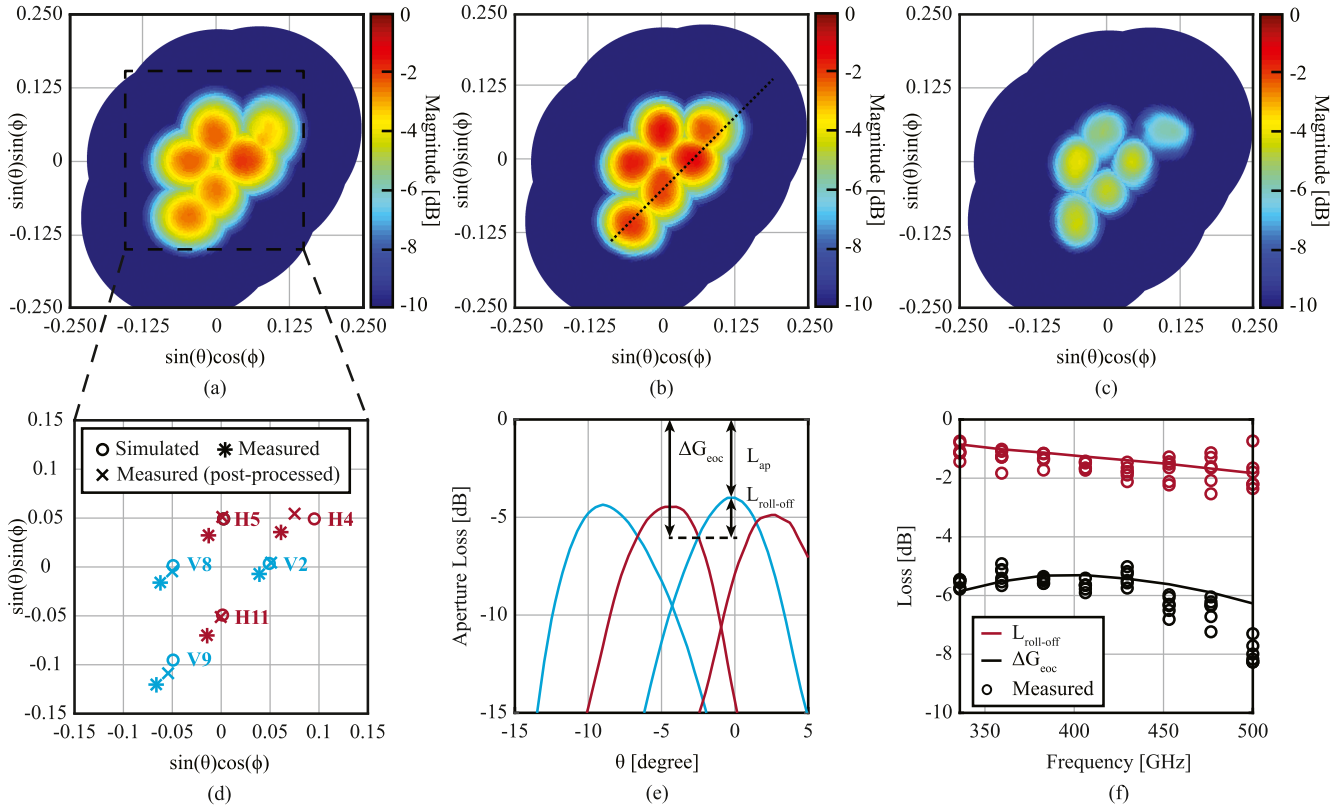

Fig. 16. (a)–(c) Interpolated measured radiation patterns of six array elements, three per polarization *H*/*V* at 325, 400, and 500 GHz, respectively. (d) Angular locations of the six beam maxima before and after the postmeasurement alignment are shown using the asterisks and crosses. The angular locations found from simulations are shown using the circles. (e) Radiation patterns along the indicated diagonal cut at 400 GHz. (f) ΔG_{eoc} and $L_{\text{Roll-off}}$ as a function of frequency for all the measured edge-of-coverage points.

in Fig. 15(a) versus bias voltage at 400 GHz and in Fig. 15(b) as a function of frequency. Although Fig. 15(a) shows that the responsivity peaks around 0.6 V, the system NEP is not necessarily minimized at this bias voltage [18]. An empirical study on this particular measurement scenario in [30] showed that a bias voltage of 1 V yields maximum DR for characterization. Therefore, when characterizing the responsivity as a function of frequency (or the radiation patterns), the bias voltage was fixed to 1 V.

The mismatch between measurements and simulations in Fig. 15(b) follows the same trend as the directivity [see Fig. 14] and, since the responsivity includes the tapering efficiency η_{Taper} (4), can most likely be attributed to the same origins. In addition, a small process variation between the SBDs (i.e., 5%), can result in a 1-dB variation in responsivity between elements [30].

The aperture efficiency of the camera was extracted from the measured responsivity using (5) and (6). Fig. 9(c) shows the result at a bias voltage of 1 V together with the simulated aperture efficiency, with which there is a good agreement. Compared to a previously demonstrated single-pixel design with the same elliptical lens and a similar direct-detector topology [18], the additional penalty in aperture efficiency arising from an array implementation is relatively small (e.g., -1 dB at 400 GHz).

From an imaging perspective, it can be interesting to translate these results in terms of NEP performance. Upon combining the NEP of the single-pixel detector [18] with the aforementioned difference in aperture efficiency, we can extrapolate that the NEP would increase from 99 to 115 pW/$\sqrt{\text{Hz}}$ at 400 GHz. Although this does not suffice for passive imaging, it can be seen that the difference between these single-pixel and FPA implementations is minor. The proposed chessboard array can be used with higher performing devices [32] or in other processes, such as SiGe [7], to improve the NEP.

C. Beam Sampling and Edge-of-Coverage Gain

Using the measurement results presented in previous sections, we can determine the angular sampling of the beams and, subsequently, the difference between the gain of an ideal aperture and the gain at the edge of coverage (ΔG_{eoc}). This is achieved by plotting all the measured radiation patterns in the same global UV reference system using the retrieved locations of the beam maxima from the alignment procedure. Fig. 16(d) displays the locations of the beam maxima in the global UV reference system at 400 GHz, where blue represents the vertically polarized elements V and red the horizontally polarized elements H. The simulated locations of the beam maxima are indicated using the circles, whereas the measured locations are indicated using the asterisks. Since the broadside direction of the lens should ideally correspond to the center of the array of accessible elements (see Fig. 1), the beam maxima associated to the central V and H elements should ideally be located in the $\phi = 0^\circ$ and 90° cuts,

TABLE II
COMPARISON OF STATE-OF-THE-ART THZ IMAGERS IN TERMS OF SAMPLING PERIODICITY, BANDWIDTH AND APERTURE EFFICIENCY IN THE MIDDLE OF THEIR OPERATIONAL FREQUENCY BAND

Reference	Technology	Array Grid	Antenna	Size	Bandwidth (Rel.)	Bandwidth (Abs.) [GHz]	Periodicity	η_{Ap} [dB]
This work	22 nm SOI CMOS	Chessboard	Dipole	$2 \times 2 \times 3$	1:3.0	200–600	$0.7F_{\#}\lambda_d$	4.1
[18]	22 nm SOI CMOS	-	Double Slot	1×1	1:3.0	200–600	$2.5F_{\#}\lambda_d$	3.0
[17], [33]	130 µm SiGe	-	Wire ring	1×1	1:2.9	350–1000 [a]	$1.2F_{\#}\lambda_d$	4.0
[6]	65 nm SOI CMOS	Rectangular	Wire ring	32×32	1:1.3	750–1000	$1.4F_{\#}\lambda_d$	3.2
[10]	65 nm SOI CMOS	Rectangular	Patch	4×4	1:1.1	270–290	$0.5\lambda_0$ [b]	5.5
[9]	130 µm SiGe	Rectangular	Wire ring	4×4	1:1.3	230–290	$0.5\lambda_0$ [b]	3.4[c]

[a] Here, 450 GHz is taken as the reference frequency, since this is were the imager reaches peak sensitivity.
[b] These works do not include a focusing element in the imaging system.
[c] Estimated from the difference between the reported detector and system NEP using (6), the authors mention a near conjugate impedance matching.

respectively. Because of the 50-µm manufacturing accuracy in the alignment cavity of the chip (see Fig. 10), a maximum error of 2° from this ideal situation can be expected.

In addition, since the *V* and *H* elements were mounted using different brackets, each with their own mechanical alignment errors, their respective beam maxima were found in separate global reference systems. To relate the *H* and *V* reference systems, the symmetry in the chessboard FPA topology was used. The global UV reference system of the *V* elements was translated in postprocessing such that the maxima of the two centrally located elements are line symmetric in the (ideal) $\phi = 90°$ cut and such that their (average) angular locations lie on the $\phi = 0°$ cut. It should be emphasized that no manipulation was applied to the angular spacing between the local reference systems within the global reference systems. The global *H* reference system was first rotated by 90° to relate it to the global *V* reference system and then translated such that the maxima of the two central *H* elements are line symmetric in the $\phi = 0°$ cut and located in the $\phi = 90°$ cut. The angular locations of the beams after the postmeasurement alignment procedure are shown in Fig. 16(d) using the crosses.

Next, the radiation patterns of the elements were normalized to the measured aperture efficiency and then interpolated to obtain the 2-D multibeam radiation pattern of the camera, as shown in Fig. 16(a)–(c). It can be seen in these figures that one of the elements in the FoV [corresponding to the pattern in Fig. 13(a)] consistently has lower aperture efficiency compared to the other elements. Considering that, of all the measured elements, this element is located closest to the chip perimeter, the performance drop of this specific element can be attributed to edge effects. By normalizing the radiation patterns to the aperture efficiency, we can directly estimate ΔG_{eoc} at the crossover between adjacent beams. In Fig. 16(e), which shows the radiation patterns along the diagonal cut in Fig. 16(b), one can recognize how the magnitude at the edge of coverage relates to ΔG_{eoc}, as defined in (2). Clearly, the beam sampling in Fig. 16(a)–(c) and (e) closely resembles the narrow spacing of the beams expected from Fig. 6(f).

The evolution of $L_{Roll\text{-}off}$ and ΔG_{eoc} over frequency between all the measured diagonally adjacent elements is shown in Fig. 16(f) together with the simulated results. Fig. 17 shows the measured ΔG_{eoc} along all the planes of the considered elements in comparison to simulations, in a similar fashion to Fig. 3. The error bars indicate the range in which ΔG_{eoc} was found at a specific frequency. It can be observed that the agreements between the measured and simulated ΔG_{eoc} are comparable to those of the directivity and aperture efficiency measurements. It is worth noting that, even including the ohmic losses introduced by the CMOS process [see Fig. 9(a)], the fabricated chessboard array has a 1.2-dB higher maximum ΔG_{eoc} compared with the ideal hexagonal array. For a chessboard array without ohmic losses, this improvement would be even 3.5 dB.

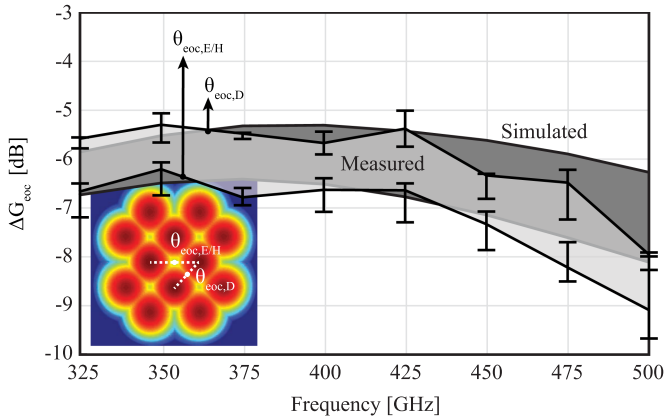

Fig. 17. Measured and simulated ΔG_{eoc} of the chessboard array configuration along measured diagonal, horizontal, and vertical cuts. The light gray band represents the measured range, whereas the dark gray band represents the simulated range, similar to Fig. 3 but including ohmic losses. The error bars indicate the maximum observed deviation from the average value.

In Table II, the performance of the chessboard array is compared with state-of-the-art integrated detector arrays operating in a similar frequency range. In addition, two single-pixel designs are also given to indicate the performance difference in terms of aperture efficiency between a single-pixel design and an array design. The chessboard array, operating from 200 to 600 GHz, has the largest relative bandwidth (3:1), and the improvement in terms of resolution (i.e., sampling periodicity) is at least a factor two compared to the other works. Moreover, the demonstrated aperture efficiency is similar to that of the state of the art, with only a 1-dB penalty with respect to the single-pixel detector from [18]. Although no ΔG_{eoc} is reported in the other works, the aforementioned observations make it safe to assume that the chessboard array is also superior in this regard to the other works in Table II.

VI. Conclusion

In this article, we demonstrated a tightly sampled chessboard FPA, operational over a 3:1 relative bandwidth, from 200 to 600 GHz, with integrated direct detectors in 22-nm FD-SOI CMOS for THz imaging applications. The tight sampling of the focal plane was implemented by utilizing two polarizations in the self-complementary chessboard array geometry and by exploiting the SiO_2 layers in the CMOS stratification to create a nonresonant leaky-wave cavity, which increases the effective area of the feed elements. To comply with the strict metal density design rules of the technology, the metal tiling was fully incorporated in the design procedure. By treating it as an artificial dielectric layer, the losses due to the metal tiling were minimized to only 0.2 dB over the entire band. Even though a close element spacing results in increased mutual coupling losses, the overall penalty in aperture efficiency was alleviated when compared to a traditional idealized hexagonal array.

An extensive measurement campaign in the WR2.2 band of a demonstrator showed that a maximum aperture efficiency of -4.1 dB was realized, which is comparable to that of state-of-the-art detector arrays and even single-pixel designs. Furthermore, the beam sampling in the FoV of the demonstrated chessboard array is near diffraction limited in the middle of the operational band, and the gain roll-off to the edge of coverage was measured to be only -1.5 dB at 400 GHz. The agreement between simulations and measurements is within 1 dB over the largest part of the WR2.2 band. Combinedly, the roll-off loss and the aperture efficiency yield a ΔG_{eoc} improvement of 1.2 dB with respect to an ideal hexagonal FPA of uniform feeds, including 2 dB of ohmic losses. Since the strict design rules of a deeply scaled CMOS node did not prohibit the realization of a high-performance antenna array, the presented concepts can also be extrapolated to other less restricting silicon platforms (such as SiGe) with potentially higher NEPs. The combination of excellent angular resolution and relatively high aperture efficiency demonstrates that the presented array design is very suitable for future commercial, passive, and high-resolution THz imaging systems.

Acknowledgment

The authors would like to thank Global Foundries for the technology access.

References

[1] K. B. Cooper et al., "THz imaging radar for standoff personnel screening," *IEEE Trans. THz Sci. Technol.*, vol. 1, no. 1, pp. 169–182, Sep. 2011.

[2] R. Appleby and H. B. Wallace, "Standoff detection of weapons and contraband in the 100 GHz to 1 THz region," *IEEE Trans. Antennas Propag.*, vol. 55, no. 11, pp. 2944–2956, Nov. 2007.

[3] P. Hillger, J. Grzyb, R. Jain, and U. R. Pfeiffer, "Terahertz imaging and sensing applications with silicon-based technologies," *IEEE Trans. THz Sci. Technol.*, vol. 9, no. 1, pp. 1–19, Jan. 2019.

[4] M. Köhler, J. Hasch, H. Bloecher, and L.-P. Schmidt, "Feasibility of automotive radar at frequencies beyond 100 GHz," *Int. J. Microw. Wireless Technol.*, vol. 5, pp. 49–54, 2013.

[5] E. Seok et al., "Progress and challenges towards terahertz CMOS integrated circuits," *IEEE J. Solid-State Circuits*, vol. 45, no. 8, pp. 1554–1564, Aug. 2010.

[6] R. Al Hadi et al., "A 1 k-pixel video camera for 0.7–1.1 terahertz imaging applications in 65-nm CMOS," *IEEE J. Solid-State Circuits*, vol. 47, no. 12, pp. 2999–3012, Dec. 2012.

[7] M. Andree, J. Grzyb, R. Jain, B. Heinemann, and U. R. Pfeiffer, "Broadband modeling, analysis, and characterization of SiGe HBT terahertz direct detectors," *IEEE Trans. Microw. Theory Techn.*, vol. 70, no. 2, pp. 1314–1333, Feb. 2022.

[8] E. Shaulov, S. Jameson, and E. Socher, "A zero bias j-band antenna-coupled detector in 65-nm CMOS," *IEEE Trans. THz Sci. Technol.*, vol. 11, no. 1, pp. 62–69, Jan. 2021.

[9] K. Sengupta, D. Seo, L. Yang, and A. Hajimiri, "Silicon integrated 280 GHz imaging chipset with 4×4 SiGe receiver array and CMOS source," *IEEE Trans. THz Sci. Technol.*, vol. 5, no. 3, pp. 427–437, May 2015.

[10] R. Han et al., "Active terahertz imaging using Schottky diodes in CMOS: Array and 860-GHz pixel," *IEEE J. Solid-State Circuits*, vol. 48, no. 10, pp. 2296–2308, Oct. 2013.

[11] G. C. Trichopoulos, H. L. Mosbacker, D. Burdette, and K. Sertel, "A broadband focal plane array camera for real-time THz imaging applications," *IEEE Trans. Antennas Propag.*, vol. 61, no. 4, pp. 1733–1740, Apr. 2013.

[12] S. van Berkel, O. Yurduseven, A. Freni, A. Neto, and N. Llombart, "THz imaging using uncooled wideband direct detection focal plane arrays," *IEEE Trans. THz Sci. Technol.*, vol. 7, no. 5, pp. 481–492, Sep. 2017.

[13] S. Dabironezare et al., "Dual band kinetic inductance bolometers for submillimeter-wave imaging: Experimental and theoretical optical response," in *Proc. 43rd Int. Conf. Infrared Millimeter THz Waves*, 2018, pp. 1–2.

[14] J. Luomahaara et al., "A passive, fully staring THz video camera based on kinetic inductance bolometer arrays," *IEEE Trans. THz Sci. Technol.*, vol. 11, no. 1, pp. 101–108, Jan. 2021.

[15] R. Zatta, V. S. Jagtap, J. Grzyb, and U. R. Pfeiffer, "CMOS camera-type THz compact antenna test range for far-field radiation pattern analysis," in *Proc. 45th Int. Conf. Infrared Millimeter THz Waves*, 2020, pp. 1–2.

[16] D. Robertson et al., "The CONSORTIS 16-channel 340 GHz security imaging radar," *Proc. SPIE*, vol. 10634, 2018, Art. no. 1063409.

[17] M. Andree, J. Grzyb, R. Jain, B. Heinemann, and U. R. Pfeiffer, "A broadband dual-polarized terahertz direct detector in a 0.13-μm SiGe HBT technology," in *Proc. IEEE MTT-S Int. Microw. Symp.*, 2019, pp. 500–503.

[18] S. V. Berkel et al., "Wideband modeling of CMOS schottky barrier diode detectors for THz radiometry," *IEEE Trans. THz Sci. Technol.*, vol. 11, no. 5, pp. 495–507, Sep. 2021.

[19] S. L. van Berkel et al., "High resolution passive THz imaging array with polarization reusage in 22nm CMOS," in *Proc. 44th Int. Conf. Infrared Millimeter THz Waves*, 2019, pp. 1–2.

[20] O. Yurduseven, D. Cavallo, A. Neto, G. Carluccio, and M. Albani, "Parametric analysis of extended hemispherical dielectric lenses fed by a broadband connected array of leaky-wave slots," *IET Microw. Antennas Propag.*, vol. 9, pp. 611–617, 2015.

[21] D. Cavallo and A. Neto, "A connected array of slots supporting broadband leaky waves," *IEEE Trans. Antennas Propag.*, vol. 61, no. 4, pp. 1986–1994, Apr. 2013.

[22] A. Neto, S. Monni, and F. Nennie, "UWB, non dispersive radiation from the planarly fed leaky lens antenna—Part II: Demonstrators and measurements," *IEEE Trans. Antennas Propag.*, vol. 58, no. 7, pp. 2248–2258, Jul. 2010.

[23] R. Carter et al., "22nm FDSOI technology for emerging mobile, Internet-of-Things, and RF applications," in *Proc. IEEE Int. Electron Devices Meeting*, 2016, pp. 2.2.1–2.2.4.

[24] S. van Berkel et al., "Wideband double leaky slot lens antennas in CMOS technology at submillimeter wavelengths," *IEEE Trans. THz Sci. Technol.*, vol. 10, no. 5, pp. 540–553, Sep. 2020.

[25] J. F. Johansson, *Millimetre Wave Imaging: Theory and Experiments*, Gothenburg, Sweden: Chalmers Univ. Technol., 1986.

[26] G. Carluccio and M. Albani, "Efficient adaptive numerical integration algorithms for the evaluation of surface radiation integrals in the high-frequency regime," *Radio Sci.*, vol. 46, no. 5, pp. 1–8, 2011.

[27] A. Garufo, N. Llombart, and A. Neto, "Radiation of logarithmic spiral antennas in the presence of dense dielectric lenses," *IEEE Trans. Antennas Propag.*, vol. 64, no. 10, pp. 4168–4177, Oct. 2016.

[28] D. Cavallo, "Analytical tool for artificial dielectric layers (ADL GUI)," 2017. [Online]. Available: https://terahertz.tudelft.nl/Research/project.php?id=114&pid=81

[29] D. Cohen and R. Shavit, "Bi-anisotropic metamaterials effective constitutive parameters extraction using oblique incidence S-parameters method," *IEEE Trans. Antennas Propag.*, vol. 63, no. 5, pp. 2071–2078, May 2015.
[30] M. Hoogelander, M. Alonso-delPino, M. Llombart, and M. Spirito, "Over-the-air characterization techniques for antenna-coupled direct-detectors at terahertz frequencies," in *Proc. IEEE MMT-S Int. Microw. Symp.*, 2023, pp. 919–921.
[31] A. Ludwig, "The definition of cross polarization," *IEEE Trans. Antennas Propag.*, vol. 21, no. 1, pp. 116–119, Jan. 1973.
[32] R. Jain, R. Zatta, J. Grzyb, D. Harame, and U. R. Pfeiffer, "A terahertz direct detector in 22 nm FD-SOI CMOS," in *Proc. 13th Eur. Microw. Integr. Circuits Conf.*, 2018, pp. 25–28.
[33] J. Grzyb, M. Andree, R. Jain, B. Heinemann, and U. R. Pfeiffer, "A lens-coupled on-chip antenna for dual-polarization SiGe HBT THz direct detector," *IEEE Antennas Wireless Propag. Lett.*, vol. 18, no. 11, pp. 2404–2408, Nov. 2019.

Martijn Hoogelander (Student Member IEEE) received the B.Sc. (*cum laude*) and M.Sc. degrees in electrical engineering in 2017 and 2021, respectively, from the Delft University of Technology (TU Delft), Delft, The Netherlands, where he is currently working toward the Ph.D. degree with the Terahertz Sensing Group.

During his master's degree, he specialized in microelectronics, with an emphasis on RF/wireless design with the Electronics Research Laboratory, TU Delft. His current research interests include passive imaging at submillimeter wavelengths and integrated circuits for antenna-coupled direct detectors.

Sven van Berkel (Member, IEEE) received the B.Sc. and M.Sc. degrees (*cum laude*) in electrical engineering in 2012 and 2015, respectively, and the Ph.D. degree (*cum laude*) in electromagnetics in 2020, all from the Delft University of Technology (TU Delft), Delft, The Netherlands.

During his master's degree, he specialized in telecommunications engineering with a focus on antennas and electromagnetic wave theory. His Ph.D. research was conducted with the Terahertz Sensing Group, TU Delft, and focused on passive imaging systems, ultrawideband antennas for millimeter- and submillimeter-wave applications, quasi-optical systems and analytical/numerical techniques in electromagnetics, and transmission line characterization. From 2020 to 2022, he was a NASA Postdoctoral Program Fellow with the Submillimeter-Wave Advanced Technology Group, NASA Jet Propulsion Laboratory (JPL), California Institute of Technology, Pasadena, CA, USA. In this fellowship, he conducted research on wideband, multibeam, and beam-scanning antenna architectures for terahertz spectroscopy instruments. Since 2022, he has been an RF Microwave Engineer with NASA JPL.

Dr. van Berkel was the recipient of the Vederprijs 2020, a Dutch award given yearly to a researcher in the field of radio and microwaves, for his Ph.D. research.

Eduard Satoshi Malotaux (Member, IEEE) was born in Geldrop, The Netherlands. He received the M.Sc. degree in electrical engineering in 2013 from the Delft University of Technology, Delft, The Netherlands, where he also worked toward the Ph.D. degree in millimeter-wave and terahertz radiameters.

In 2020, he joined Tusk IC, Antwerp, Belgium, where he currently works on the design of custom millimeter-wave ICs. His current research interests include millimeter-wave and submillimeter-wave integrated circuits, antennas, devices, systems, packaging, characterization, and measurements.

Maria Alonso-delPino (Senior Member, IEEE) received the degree in telecommunications engineering from the Technical University of Catalonia (UPC), Barcelona, Spain, in 2008, the M.S. degree in electrical engineering from the Illinois Institute of Technology, Chicago, IL, USA, in 2008, and the Ph.D. degree in signal theory and communications/electrical engineering from UPC in 2013.

From 2014 to 2015, she was a Postdoctoral Researcher with the Delft University of Technology (TU Delft), Delft, The Netherlands. From 2015 to 2016, she was a NASA Postdoctoral Fellow with Jet Propulsion Laboratory (JPL), Pasadena, CA, USA. From 2016 to 2020, she was a Member of the Technical Staff with the Sub-millimeter Wave Advanced Technology Group of JPL/NASA. Since 2020, she has been an Assistant Professor with TU Delft. Her research interests include millimeter- and submillimeter-wave heterodyne and direct detection receiver technologies, antennas, and quasi-optical systems.

Dr. Alonso-delPino was the recipient of the Outstanding Reviewer Award of IEEE TRANSACTIONS ON TERAHERTZ SCIENCE AND TECHNOLOGY in 2013, a corecipient of the 2014 IEEE Terahertz Science and Technology Best Paper Award in 2014, and a corecipient of the European Conference on Antennas and Propagation Best Antenna Design Paper Award in 2022.

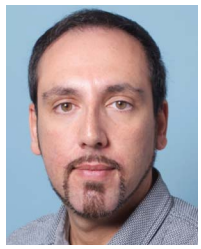

Daniele Cavallo (Senior Member, IEEE) received the M.Sc. degree (*summa cum laude*) in telecommunication engineering from the University of Sannio, Benevento, Italy, in 2007, and the Ph.D. degree (*cum laude*) in electromagnetics from the Eindhoven University of Technology, Eindhoven, The Netherlands, in 2011.

From 2007 to 2011, he was with the Antenna Group, Netherlands Organization for Applied Scientific Research, The Hague, The Netherlands. From 2012 to 2015, he was Postdoctoral Researcher with the Microelectronics Department, Delft University of Technology (TU Delft), Delft, The Netherlands. In 2015, he joined the Chalmers University of Technology, Gothenburg, Sweden, as a Visiting Researcher. He is currently an Associate Professor with the Terahertz Sensing Group, TU Delft. He has authored or coauthored about 180 papers published in peer-reviewed international journals and conference proceedings. His current research interests include analytical and numerical methods for antenna modeling, design of antenna arrays, and on-chip antennas.

Dr. Cavallo was a recipient of the Best Innovative Paper Prize at the European Space Agency Antenna Workshop in 2008, the Best Paper Award in Electromagnetics and Antenna Theory at 11th European Conference on Antennas and Propagation (EuCAP) in 2017, and the 250 keuro "Veni" Personal Grant from the Netherlands Organization for Scientific Research in 2015. His students received the Best Student Paper Award at EuCAP 2013, the Special Mention at EuCAP 2015, the Else Kooi Prize in 2016, and the Honorable Mention at IEEE Antennas and Propagation Society International Symposium in 2019. He is a Member of the European Association on Antennas and Propagation (EurAAP), the co-coordinator of the EurAAP working group "Active Array Antennas," and a Management Committee Member of the COST Action "Future communications with higher-symmetric engineered artificial materials (SyMat)." He has served as an Associate Editor for IEEE TRANSACTIONS ON ANTENNAS AND PROPAGATION from 2016 to 2022.

Marco Spirito (Member, IEEE) received the M.Sc. degree (*cum laude*) in electrical engineering from the University of Naples Federico II, Naples, Italy, in 2000, and the Ph.D. degree in microelectronics from the Delft University of Technology, Delft, The Netherlands, in 2006.

From 2000 to 2001, he was a Guest Researcher with Infineon Technologies, Munich, Germany. In 2006, he joined the Department of Electronics and Telecommunications Engineering, University of Naples Federico II. In 2008, he joined the Electronics Research Laboratory, Delft University of Technology, as an Assistant Professor, where he has been an Associate Professor since April 2013. In 2010 and 2017, he was one of the co-founders of Anteverta-MW, Eindhoven, The Netherlands, and Vertigo Technologies, Delft, respectively, two companies pioneering innovative measurement techniques and instruments. His research interests include the development of advanced passive components and building blocks operating in the millimeter and submillimeter frequency ranges, the development of characterization setups and calibration techniques for millimeter and submillimeter waves, and the design and integration of millimeter-wave sensing systems.

Dr. Spirito was a recipient of the Best Student Paper Award for his contribution to 2002 IEEE Bipolar/BiCMOS Circuits and Technology Meeting. He received the IEEE Microwave Theory and Techniques Society Microwave Prize in 2008. He was a corecipient of the Best Student Paper Award at 2011 IEEE Radio Frequency Integrated Circuits Symposium, the GAAS Association Student Fellowship in 2012, the Best Student Paper Award in second place at 2018 International Microwave Biomedical Conference, the Best Paper Award at 2019 Winter Automatic RF Techniques Group (ARFTG) Conference, and the Best Student Paper Award at 2019 Summer ARFTG Conference.

Nuria Llombart (Fellow, IEEE) received the master's degree in electrical engineering and the Ph.D. degree in electromagnetics from the Polytechnic University of Valencia, Valencia, Spain, in 2002 and 2006, respectively.

During her master's degree studies, she spent one year with the Friedrich Alexander University of Erlangen Nuremberg, Erlangen, Germany, and worked with the Fraunhofer Institute for Integrated Circuits, Erlangen. From 2002 to 2007, she was with the Antenna Group, TNO Defense, Security and Safety Institute, The Hague, The Netherlands, working as a Ph.D. student and afterward as a Researcher. From 2007 to 2010, she was a Postdoctoral Fellow with the Submillimeter Wave Advance Technology Group, Jet Propulsion Laboratory, California Institute of Technology, Pasadena, CA, USA. She was a "Ramón y Cajal" Fellow with the Optics Department, Complutense University of Madrid, Madrid, Spain, from 2010 to 2012. In 2012, she joined the THz Sensing Group, Technical University of Delft, Delft, The Netherlands, where she has been a Full Professor since February 2018. She has coauthored more than 200 journal and international conference contributions in the areas of antennas and terahertz (THz) systems.

Dr. Llombart was the corecipient of the H. A. Wheeler Award for the Best Applications Paper of 2008 in IEEE TRANSACTIONS ON ANTENNAS AND PROPAGATION, the 2014 THz Science and Technology Best Paper Award of the IEEE Microwave Theory and Techniques Society, and several NASA awards. She was also the recipient of the 2014 IEEE Antenna and Propagation Society Lot Shafai Mid-Career Distinguished Achievement Award. In 2015, she was the recipient of European Research Council Starting Grant. She is a Board Member of the International Society of Infrared, Millimeter, and Terahertz Waves and an Associate Editor for IEEE TRANSACTIONS ON ANTENNAS AND PROPAGATION. In 2019, she became IEEE fellow for contributions to millimeter and submillimeter wave quasi-optical antennas.